Author/s:
Wu, C;Blunck, Y;Johnston, LA

Title:
The “Spin-3/2 Bloch Equation”: System matrix formalism of excitation, relaxation, and off-resonance effects in biological tissue

Date:
2022-09-01

Citation:
Wu, C., Blunck, Y. & Johnston, L. A. (2022). The “Spin-3/2 Bloch Equation”: System matrix formalism of excitation, relaxation, and off-resonance effects in biological tissue. Magnetic Resonance in Medicine, 88 (3), pp.1370-1379. https://doi.org/10.1002/mrm.29276.

Persistent Link:
https://hdl.handle.net/11343/336486

The 'Spin-3/2 Bloch Equation': System matrix formalism of excitation, relaxation and off-resonance effects in biological tissue

Journal:	*Magnetic Resonance in Medicine*
Manuscript ID	MRM-21-22659.R2
Wiley - Manuscript type:	Technical Note
Research Type:	Theoretical < Technical Research, Na-23 < Non-proton techniques < Technique Development
Research Focus:	No specific tissue or organ focus

The 'Spin-3/2 Bloch Equation': System matrix formalism of excitation, relaxation and off-resonance effects in biological tissue

Chengchuan Wu[1,2*], Yasmin Blunck[1,2], Leigh A. Johnston[1,2]

1 Melbourne Brain Centre Imaging Unit, The University of Melbourne, Parkville, VIC, Australia

2 Department of Biomedical Engineering, The University of Melbourne, Parkville, VIC, Australia

***** Corresponding author: Chengchuan Wu, Melbourne Brain Centre Imaging Unit, Kenneth Myer Building, 30 Royal Parade, Parkville, VIC, 3010, Australia.
Email: chengchuanw@student.unimelb.edu.au

Manuscript word count: 2661
Abstract word count: 224

Abstract

Purpose: This work proposes 'Spin-3/2 Bloch Equation' (SBE), a consolidated formalism for spin-3/2 dynamics in biological environments.. The formalism encapsulates excitation, relaxation and off-resonance with accessible matrix representation for a straightforward implementation with high computational efficiency.

Theory: The SBE is derived using spherical tensor operators to encapsulate the spin-3/2 dynamics in biological systems in a single system matrix, a formalism akin to the well-known Bloch Equations (BE).

Methods: Using the proposed SBE, simulations of three classical ^{23}Na pulse sequences were performed to demonstrate the versatility and applicability of the model, returning the evolution of the ^{23}Na spin system during these experiments: soft rectangular and adiabatic inversion recovery (IR) and triple-quantum filtering. IR simulations were compared with two existing spin-3/2 simulators and the adaptive BE as a first-order approximation.

Results: The proposed SBE is straightforward to implement and facilitates accurate and fast simulations of the underlying higher order coherence in sodium experiments of biological tissues. SBE simulations and comparison spin-3/2 simulators outperform the BE simulations as expected, with the SBE offering superior computational efficiency achieved by the single system matrix formalism.

Conclusion: The proposed SBE enables comprehensive and accurate simulations for spin-3/2 systems in biological tissue. With a one-line call to an ODE solver, it offers a computationally efficient and accessible method for use in ^{23}Na pulse sequence design.

Keywords: sodium (^{23}Na); NMR; MRI; tensor operator; relaxation; simulation

Introduction

The sodium isotope ^{23}Na, with nearly 100% abundance, is the second largest NMR signal source in-vivo and offers great potential for non-proton imaging in basic and clinical research studies as a sensitive biomarker of tissue viability and organ function (1–3). In particular, ^{23}Na MRI techniques targeting intracellular sodium are demonstrating promising outcomes: adiabatic inversion recovery (IR) has been used to quantify sodium in knee cartilage, with the potential to diagnose osteoarthritis (4); simultaneous single-quantum- and triple-quantum-filtered imaging has been demonstrated in the prediction of gene mutation of cerebral gliomas (5).

Simulation is an important tool in ^{23}Na MRI sequence design and analysis, the basis of which is the chosen spin-3/2 dynamics formalism determining the mathematical expansion of the Liouville-von Neumann equation. Various formalisms have been derived dependent on the motivation of the study; for simulations concerning sequences with short and strong RF pulses, a hard-pulse approximation is typically made to obtain a closed form expression of the spin dynamics. These approaches model selected experiments such as triple-quantum filtering (TQF) (6–8) and steady-state free precession (9). For spin-3/2 dynamics under modulated RF pulses, the spin-1/2 Bloch Equation (BE) can be used as a first-order approximation (10, 11). While accurately describing the spin-3/2 behaviour in fast-motion environments such as fluid, the BE does not capture multiple-quantum coherences and the quadrupolar decay in slow-motion environments. In order to obtain a more accurate description that reduces approximation error of the simulations, a spin-3/2 formalism incorporating relaxation and excitation was proposed by Hancu et al (12). This formalism has since been widely used to investigate the relaxation impacts on the signal (12, 13), simulations of long pulses (14–16) and pulse trains (17, 18).

A key step in the derivation of an explicit formalism is the secularisation process in which the time dependency of the relaxation function is removed in order to obtain an expression for the relaxation. For spin-3/2 dynamics in condensed matter, secularisation has been carried out based on Redfield theory (12, 19, 20). This widely used derivation is confined to specific conditions, for example on-resonance RF fields applied to anisotropic environments, and off-resonance RF applied to isotropic environments. It has remained unclear whether the secularised expression is valid under the arbitrary conditions.

The purpose of the current paper is to propose a generalised algebraic formalism representative of spin-3/2 systems in biological tissue, including relaxation during RF in isotropic and anisotropic media as well as a complete consideration of off-resonance effects in the secularisation process. We consolidate the treatment based on the irreducible spherical tensor operator (ISTO) and compile previously specific and isolated forms into a generalised system matrix equation, which we herein refer to (albeit somewhat facetiously) as the 'Spin-3/2 Bloch Equation' (SBE), with obvious analogy to the BE algebraic model of bulk magnetisation in biological tissue for spin-1/2 nuclei. The SBE system matrix enables full simulation of spin-3/2 dynamics in any numerical environment with

a single call to a numerical integration function, obviating the need for piecewise treatment of excitation, relaxation and off-resonance embedded in previous ISTO-based simulators (1, 18). While the demonstrations and discussion of SBE are focused on ^{23}Na imaging, the formalism can also apply to other MR-observable spin-3/2 nuclei, such as ^{35}Cl and ^{39}K.

The properties of the SBE are expounded by the generation of three types of ^{23}Na MRI sequences: soft rectangular pulse inversion, adiabatic inversion and triple-quantum filtering. This demonstrates the broad applicability of the proposed SBE framework across a wide range of sodium pulse sequences and provides insight into the deviation of the spin-3/2 system dynamics from their spin-1/2 system counterpart. Accuracy, computational efficiency and generalisability of SBE simulations are illustrated through MATLAB-based comparison with the Madelin et al (1) and Kratzer et al (18) ISTO-based simulators.

Theory

In this work, all physical quantities are described in the RF rotating frame. The dynamics of the density operator, $\hat{\rho}$, can be described by the master equation incorporating the Redfield relaxation function, $\hat{\Gamma}$ (21),

$$\frac{d}{dt}\hat{\rho}(t) = -i[\hat{H}_D, \hat{\rho}(t)] - \hat{\Gamma}\left(\hat{\rho}(t) - \hat{\rho}_0\right), \qquad [1]$$

where $\hat{\rho}_0$ denotes the density operator at thermal equilibrium and $\hat{H}_D$ denotes the Hamiltonian of deterministic propagation, consisting of three terms,

$$\hat{H}_D = \hat{H}_\Delta + \hat{H}_1 + \hat{H}_{QS}. \qquad [2]$$

Here, $\hat{H}_\Delta$, $\hat{H}_1$ and $\hat{H}_{QS}$ derive from the effective static magnetic field, the RF field and the time-averaged quadrupolar electric field gradient (EFG), respectively.

The relaxation function describes the interaction with the fluctuating quadrupolar Hamiltonian, $\hat{H}_{QF}$ (19),

$$\hat{\Gamma}\left(\hat{\rho}(t) - \hat{\rho}_0\right) = \int_0^\infty \left[\hat{H}_{QF}(t), \left[\exp\left\{-i\hat{H}_D\tau\right\}\hat{H}_{QF}(t-\tau)\exp\left\{i\hat{H}_D\tau\right\}, \hat{\rho}(t) - \hat{\rho}_0\right]\right] d\tau. \qquad [3]$$

The SBE is a matrix representation of the master equation, Eq. 1,

$$\frac{d}{dt}\mathbf{P} = \mathbf{L}\mathbf{P} + \mathbf{C}. \qquad [4]$$

where $\mathbf{L}$ is the system matrix and $\mathbf{C}$ the offset vector arising from $\hat{\rho}_0$ for system state $\mathbf{P}$ (i.e. the vector representation of $\hat{\rho}$). ISTO has been chosen as the basis for Eq. 4. The orthonormal unit tensor operator, denoted as $\hat{T}_{lm}$, represents the component of rank l and coherence m. A set of 16 ISTOs, with $l = 0, 1, 2, 3$, $m = 1, \ldots, l$, form a complete space for spin-3/2. Furthermore, we can transform the ISTOs into the symmetric (s) and antisymmetric (a) combinations, by

$$\hat{T}_{lm}(s) = \frac{1}{\sqrt{2}}\left(\hat{T}_{l-m} + \hat{T}_{lm}\right) \qquad [5a]$$

$$\hat{T}_{lm}(a) = \frac{1}{\sqrt{2}}\left(\hat{T}_{l-m} - \hat{T}_{lm}\right), \quad [5b]$$

so that $\hat{T}_{11}(a)$, $\hat{T}_{11}(s)$ and $\hat{T}_{10}$ are proportional to the x-, y- and z-magnetisation, respectively. Moreover, as far as most NMR and MRI applications are concerned, we can omit the $\hat{T}_{00}$ because it has no contribution to the contrast in an isolated spin ensemble. Here, we define the basis for Eq. 4 as

$$\left\{\hat{T}_{10}, \hat{T}_{11}(a), \hat{T}_{11}(s), \hat{T}_{20}, \hat{T}_{21}(a), \hat{T}_{21}(s), \hat{T}_{22}(a), \hat{T}_{22}(s), \hat{T}_{30}, \hat{T}_{31}(a), \hat{T}_{31}(s), \hat{T}_{32}(a), \hat{T}_{32}(s), \hat{T}_{33}(a), \hat{T}_{33}(s)\right\}. \quad [6]$$

The SBE system matrix $\mathbf{L}$ is parameterised by RF amplitude (nutation frequency), $\omega_1(t)$, the initial RF phase, ϕ_0 with reference to the x′-axis, off-resonance frequency, $\omega_\Delta(t)$, time-average residual quadrupolar frequency, ω_Q, and spectral densities, J_0, J_1 and J_2. Entries of $\mathbf{L}$ are colour-coded in Fig. 1 in order to provide intuitive understanding of the origins of the terms.

In order to present a derivation of this formulation of $\mathbf{L}$, consider the decomposition of the system matrix,

$$\mathbf{L} = \mathbf{D} + \mathbf{R}, \quad [7]$$

into the commutation component, $\mathbf{D}$, and the relaxation component, $\mathbf{R}$.

The Commutation Component, D

The commutation matrix, $\mathbf{D}$, contains the deterministic spin dynamics, i.e. nutation, free precession and the time-average quadrupolar coupling. By definition,

$$\begin{aligned}\mathbf{D} &\triangleq -i[\hat{H}_D, \mathbf{E}] \\ &= -i\left[\sqrt{5}\omega_\Delta \hat{T}_{10} + \sqrt{5}\omega_1 e^{i\phi_0}\hat{T}_{11}(a) + \omega_Q \hat{T}_{20}, \mathbf{E}\right] \\ &= -i\left[\sqrt{5}\omega_\Delta \hat{T}_{10}, \mathbf{E}\right] - i\left[\sqrt{5}\omega_1 e^{i\phi_0}\hat{T}_{11}(a), \mathbf{E}\right] - i\left[\omega_Q \hat{T}_{20}, \mathbf{E}\right],\end{aligned} \quad [8]$$

where $\mathbf{E}$ is the identity matrix and is equivalent to the sum of the ISTO units. The matrix form of $\mathbf{D}$ is obtained by expansion of the commutators using commutation laws (19, 22, 23).

The non-zero elements of $\mathbf{D}$ are identified in Fig. 1 by shading: off-resonance precession (yellow), nutation (red), and static quadrupolar coupling (green).

The Relaxation Component, R

The relaxation function takes the following form with $\hat{H}_{QF}$ expressed in the tensor operator basis (12):

$$\hat{\Gamma}(\hat{\rho}) = -\int_0^\infty \sum_{m=-2}^{2}\left[\hat{T}_{2m}, \left[e^{-i\hat{H}_D\tau}\hat{T}_{2m}^\dagger e^{i\hat{H}_D\tau}, \hat{\rho}\right]\right] \chi^2\langle\left[F_{2m}^*(t) - \left\langle F_{2m}^*\right\rangle\right]\left[F_{2m}(t-\tau) - \langle F_{2m}\rangle\right]\rangle e^{im\omega_r\tau}d\tau, \quad [9]$$

where $\hat{T}_{2m}^{\dagger} = (-1)^m \hat{T}_{2-m}$, χ is the quadrupolar coupling constant, F_{2m} is the EFG tensor component, ω_r is the frequency of the rotating frame with respect to the laboratory frame, and $\langle\cdot\rangle$ and $*$ denote motion average and complex conjugation, respectively.

The integral in Eq. 9 is intractable except in certain cases. To the best of our knowledge, there is no matrix representation in the literature for the generalised case when $\hat{H}_\Delta$, $\hat{H}_1$ and $\hat{H}_{QS}$ co-exist. Here, we demonstrate that, given any practical $\hat{H}_D$ for ^{23}Na NMR in biological tissue environments, $\mathbf{R}$ has the same form as the case when $\hat{H}_D$ is absent, resulting in the relaxation matrix given by the blue shaded entries in Fig. 1.

To demonstrate that relaxation rates are decoupled from the RF field, off resonance and anisotropy of the environment for ^{23}Na spin systems in biological tissue, consider the spectral density (19),

$$J(\omega) = \frac{(2\pi)^2}{20} \frac{\chi^2 \tau_c}{1 + (\omega\tau_c)^2}, \qquad [10]$$

where τ_c is the correlation time. $J(\omega)$ has been shown to be a good approximation to the integral (19)

$$J(\omega) \approx \int_0^\infty \chi^2 \langle \left[F_{2m}^*(t) - \left\langle F_{2m}^* \right\rangle\right] \left[F_{2m}(t-\tau) - \langle F_{2m}\rangle\right] \rangle e^{i\omega\tau} d\tau. \qquad [11]$$

This approximation will be used in the simplification of the relaxation function, Eq. 9. Considering now the argument of the double commutator of the relaxation function, the term $e^{-i\hat{H}_D\tau}\hat{T}_{2m}^{\dagger} e^{i\hat{H}_D\tau}$ represents the evolution of $T_{2m}^{\dagger}$ under the influence of $\hat{H}_D$. The corresponding dynamic equation is

$$\frac{d}{dt}\mathbf{T} = \mathbf{D}\mathbf{T}, \qquad [12]$$

where $\mathbf{T}$ is an arbitrary quantity in ISTO space. The term $e^{-i\hat{H}_D\tau}\hat{T}_{2m}^{\dagger} e^{i\hat{H}_D\tau}$ is equivalent to the integral of Eq. 12 over $[0, \tau]$ with the initial condition $\mathbf{T}(0) = \hat{T}_{2m}^{\dagger}$. Note that $\mathbf{D}$ is skew-Hermitian and is therefore diagonalisable with purely imaginary eigenvalues. Eq. 12 can be rewritten as

$$\frac{d}{dt}\mathbf{T} = \mathbf{Q}^{-1} \begin{bmatrix} i\lambda_1 & & \\ & \ddots & \\ & & i\lambda_{15} \end{bmatrix} \mathbf{Q}\mathbf{T}, \qquad [13]$$

where λ_k's are the eigenvalues and $\mathbf{Q}$ is the eigenvector matrix. By defining $[q_{1,s}, \ldots, q_{15,s}]^\top$ as the s-th column of $\mathbf{Q}$ corresponding to the initial condition such that $\mathbf{T}_s = \hat{T}_{2m}$, we obtain the expression

of the term $e^{-i\hat{H}_D\tau}\hat{T}_{2m}^{\dagger}e^{i\hat{H}_D\tau}$ in the $\left\{\hat{T}_{lm}\right\}$ basis,

$$\begin{aligned} e^{-i\hat{H}_D\tau}\hat{T}_{2m}^{\dagger}e^{i\hat{H}_D\tau} &= \mathbf{Q}^{-1}\begin{bmatrix} (-1)^m q_{1,s}e^{i\lambda_1\tau} \\ \vdots \\ (-1)^m q_{15,s}e^{i\lambda_{15}\tau} \end{bmatrix} \\ &= \frac{1}{\det(\mathbf{Q})}\begin{bmatrix} Q_{1,1} & \cdots & Q_{15,1} \\ \vdots & \ddots & \vdots \\ Q_{1,15} & \cdots & Q_{15,15} \end{bmatrix}\begin{bmatrix} (-1)^m q_{1,s}e^{i\lambda_1\tau} \\ \vdots \\ (-1)^m q_{15,s}e^{i\lambda_{15}\tau} \end{bmatrix} \\ &= \frac{1}{\det(\mathbf{Q})}\begin{bmatrix} (-1)^m \sum_k Q_{k,1}q_{k,s}e^{i\lambda_k\tau} \\ \vdots \\ (-1)^m \sum_k Q_{k,15}q_{k,s}e^{i\lambda_k\tau} \end{bmatrix} \\ &= \sum_{l=1}^{3}\sum_{n=-l}^{l}\sum_{k=1}^{15}\alpha_{klmn}e^{i\lambda_k\tau}\hat{T}_{ln}, \end{aligned} \quad [14]$$

where α_{klmn} is introduced to denote the coefficient. By the properties of Laplacian expansion (24),

$$\sum_k \alpha_{klmn} = \begin{cases} (-1)^m & \text{when } l = 2 \text{ and } n = m; \\ 0 & \text{otherwise.} \end{cases} \quad [15]$$

Substituting Eq. 14 into Eq. 9, we have

$$\hat{\Gamma}(\hat{\rho}) = -\sum_{m=-2}^{2}\left[\hat{T}_{2m}, \left[\sum_{l,n}\sum_k \alpha_{klmn}J(m\omega_r + \lambda_k)\hat{T}_{ln}, \hat{\rho}\right]\right]. \quad [16]$$

The spectral density function can be approximated by observation that the eigenvalues are upper-bounded such that (25)

$$\lambda_k \leq 15\max\left(|d_{ij}|\right), \quad [17]$$

where d_{ij} are the elements of $\mathbf{D}$ dependent on ω_1, ω_Δ or ω_Q (red, yellow and green shaded entries in Fig.1). In biological MR experiments, λ_k ranges between $0 \sim 10^4$ Hz, much smaller than τ_c^{-1} (26, 27), resulting in $\lambda_k\tau_c \ll 1$. In addition, $\omega_r \approx \omega_0$. We have $J(m\omega_r + \lambda_k) \approx J(m\omega_0)$ (also denoted as J_m). Hence,

$$\begin{aligned} \hat{\Gamma}(\hat{\rho}) &\approx -\sum_{m=-2}^{2}\left[\hat{T}_{2m}, \left[\sum_{l,n}\sum_k \alpha_{klmn}J_m\hat{T}_{ln}, \hat{\rho}\right]\right] \\ &= -\sum_{m=-2}^{2}\left[\hat{T}_{2m}, \left[\sum_{l,n}\sum_k \alpha_{klmn}\hat{T}_{ln}, \hat{\rho}\right]\right]J_m \\ &= -\sum_{m=-2}^{2}\left[\hat{T}_{2m}, \left[\hat{T}_{2m}^{\dagger}, \hat{\rho}\right]\right]J_m. \end{aligned} \quad [18]$$

The double commutator in Eq. 18 now can be expanded using the commutation law (19). The resultant form of Eq. 18 implies that the relaxation rates are decoupled from the RF field, the off resonance and the anisotropy of the environment when the correlation time is sufficiently short.

The Offset Vector, C

At thermal equilibrium, $\hat{\rho}_0 = \mathbf{P}(0) = \hat{T}_{10}$, resulting in the offset vector of $\mathbf{C} = -\mathbf{RP}(0)$,

$$\mathbf{C} = \left[\frac{2}{5}J_1 + \frac{8}{5}J_2, 0, 0, 0, 0, 0, 0, 0, \frac{4}{5}J_1 - \frac{4}{5}J_2, 0, 0, 0, 0, 0, 0\right]^\top. \quad [19]$$

The 'Adapted' BE

The well-known BE describes the simultaneous effects of excitation, precession and relaxation as the dynamics of a magnetisation vector, written as

$$\frac{d}{dt}\begin{bmatrix} M_x \\ M_y \\ M_z \end{bmatrix} = \begin{bmatrix} -T_2^{-1} & -\omega_\Delta & \omega_1 \sin\phi_0 \\ \omega_\Delta & -T_2^{-1} & -\omega_1 \cos\phi_0 \\ -\omega_1 \sin\phi_0 & \omega_1 \cos\phi_0 & -T_1^{-1} \end{bmatrix}\begin{bmatrix} M_x \\ M_y \\ M_z \end{bmatrix} + \begin{bmatrix} 0 \\ 0 \\ T_1^{-1} \end{bmatrix}. \quad [20]$$

The adapted BE for the spin-3/2 dynamics is the weighted linear combination of the short and long components,

$$\mathbf{M}(t) = 0.6\mathbf{M}_s(t) + 0.4\mathbf{M}_l(t), \quad [21]$$

where $\mathbf{M}_s$ and $\mathbf{M}_l$ is each a solution to BE with short and long T2, respectively. The short and long transverse relaxation times, T_{2s} and T_{2l}, have the following relationship with the spectral densities:

$$T_{2s} \approx \frac{1}{J_0 + J_1}, \quad T_{2l} = \frac{1}{J_1 + J_2} \quad when \quad \omega_Q < J_2, \quad [22a]$$

$$T_{2s} = \frac{1}{J_0 + J_1 + J_2}, \quad T_{2l} = \frac{1}{J_1 + J_2} \quad when \quad \omega_Q \geq J_2. \quad [22b]$$

Methods

Numerical integration was used to solve the SBE and BE in MATLAB (Mathworks, Natick, MA) using the Runge-Kutta method (ode45). The complete script is available at `https://github.com/MBCIU/Sodium_spin_dynamics_simulation`. SBE simulations were compared with the MATLAB-based spin-3/2 simulators of Kratzer et al (18) and Madelin et al (1), as well as the adapted BE.

Three types of motion regimes mimicking biological environments were chosen with measured spectral density values taken from Wilferth et al (28):

1. **50 mM saline (isotropic, fast-motion regime):** $J_0 = J_1 = J_2 = 8.9$ Hz, $\omega_Q = 0$ Hz, $T_1 = T_{2s} = T_{2l} = 56.1$ ms;
2. **8% agar (isotropic, slow-motion regime):** $J_0 = 250$ Hz, $J_1 = 45.4$ Hz, $J_2 = 19.3$ Hz, $\omega_Q = 0$ Hz, $T_1 = 21.7$ ms, $T_{2s} = 3.4$ ms, $T_{2l} = 15.4$ ms;
3. **3% xanthan (anisotropic, slow-motion regime):** $J_0 = 319$ Hz, $J_1 = 28.2$ Hz, $J_2 = 28.1$ Hz, $\omega_Q = 61.8$ Hz, $T_1 = 17.3$ ms, $T_{2s} = 2.7$ ms, $T_{2l} = 17.8$ ms.

Pulse Duration Effect on Magnetisation Inversion

The quadrupolar relaxation effect is known to be significant in soft rectangular inversion pulses (14). To compare the simulators in characterising the simultaneous effects of the spin-3/2 dynamics, rectangular inversion pulses with various durations were simulated, ranging from 0.5 ms to 20 ms.

Adiabatic Inversion Pulse

To examine the response of the ^{23}Na spin system to modulated pulses, the adiabatic Wide-band Uniform Rate and Smooth Truncation (WURST) inversion pulse sequence (11) was simulated.

The amplitude of the pulse is modulated by

$$\omega_1(t) = 2\pi v_1 \left(1 - \left|\sin\left(\frac{\pi(2t - T_p)}{2T_p}\right)\right|^{20}\right), \quad [23]$$

where v_1 is the amplitude in Hz and the pulse duration T_p was chosen to be 10 ms. The frequency of the pulse is given by

$$\phi(t) = \frac{\pi \Delta f}{T_p} t^2, \quad [24]$$

where the frequency sweep range, Δf, was chosen to be 2 kHz.

While SBE's implementation uses ode45 for an efficient computation of the simulation, other 3/2-spin simulators employ user-defined, linear time-steps during their calculations. To compare accuracy and performance of the simulators, WURST simulations were run across a range of step sizes for the Madelin and Kratzer simulators, in order to compare accuracy and computational efficiency with the SBE approach.

Triple-Quantum Filtering

To examine multiple-quantum coherences, a six-step TQF experiment was simulated, following the three-pulse experiment setup in Hancu et al (29), employing hard pulses of 500 μs. The first pulse was phase cycled through 30°, 90°, 150°, −150°, −90°, −30°. After the preparation time of 3 ms, the second pulse was applied with a phase offset of 90° with reference to the first pulse. The third pulse followed after a 400μs delay with phase of 0°.

Results

Pulse Duration Effect on Magnetisation Inversion

The resultant longitudinal magnetisation evolutions during the 10-ms rectangular pulse are identical in saline, while the results from adapted BE deviate from the others in agar and, more manifestly, xanthan (Fig. 2a). The differences between the spin-3/2 simulators and BE in the inverted longitudinal magnetisation amplitude are negligible when the pulse is short, but become more notable with increasing pulse length, except for saline in which there is no difference (Fig. 2b). The results obtained by the spin-3/2 simulators are in agreement. Their output of time evolution trajectories under the 10-ms rectangular pulse (Fig. 2a) agree well with the literature (14).

Adiabatic Inversion Pulse

Simulations of magnetisation evolution during WURST inversion were compared. Again, the results are identical in saline. However, the differences between the spin-3/2 simulators and BE are less obvious in agar and xanthan (Fig. 3a), compared to the results for the 10-ms soft pulse inversion in the previous simulation.

The results of the SBE, Madelin and Kratzer spin-3/2 simulators are in strong alignment with one another (Fig. 3), when the number of time steps is large for the latter two simulators. Comparing the simulation results of simulators with linearly discretised time steps shows variations in the calculated magnetisation evolution, with more time steps, i.e. small step sizes, resulting in curves that approach SBE's output. Comparison of computational times of the spin-3/2 simulators (Table 1) highlights the computational efficiency of SBE with its simulations being more than 10 times faster for simulations with high accuracy.

To demonstrate the capability of SBE, the inversion preparation stage of the WURST sequence was simulated with off-resonance frequencies ranging from -50 to 50 Hz (Fig. 3c). The longitudinal magnetisation amplitude at the end of the inversion preparation stage is shown in Fig. 3d. These results can be used to assess robustness against B_0 inhomogeneity and are in agreement with the literature (11).

Triple-quantum Filtering

TQF experiments constitute a significant aspect of spin-3/2 simulation and are the basis of TQF experiment design and signal analysis. As has been previously shown by Hancu et al (12) and Tsang et al (13) for an ISTO framework, we demonstrate the ability of SBE to provide the time evolution of all ranks and coherences of the spin-3/2 dynamics (Fig. 4a-h and Supporting Information Fig. S1). The filtered outcome, which is the sum of the phase cycling steps with proper polarity toggling, clearly exhibits the rise of the observable signal (the rank-1 order-1 component) transferred from

the rank-3 order-3 component as shown in Fig. 4i.

Discussion

Based on the ISTO formalism for convenient description of spin-3/2 dynamics, we have shown that the Redfield equation can be simplified under the condition that the correlation time is sufficiently short, which is satisfied for ^{23}Na in biological tissue. This theoretical result implies that the RF field, the off resonance and the anisotropy of the biological tissue have vanishing effect on the relaxation rates. This leads to a generalised description of the ^{23}Na spin system; the SBE captures the combined effect of the residual Zeeman field, the RF field, and the static and fluctuating components of EFG. Noticeably, incorporating relaxation under an off-resonance RF, facilitates simulation of experiments such as spin locking, adiabatic RF irradiation and slice selective excitation. Although we restrict the discussion to ^{23}Na nuclei in this paper, the formalism is extendable to other spin-3/2 nuclei as long as the correlation time condition is satisfied.

The SBE system matrix, **L**, is a structured, intuitive and accessible representation of sodium dynamics for the MRI research community that will enable advances in ^{23}Na pulse and pulse sequence design. It obviates the need for a piecewise treatment to analyse ^{23}Na sequences, with simulation rendered trivial; SBE simulation requires only the specification of the environment parameters, the pulse and gradient functions. The ability to simulate the spin-3/2 dynamics with a single call to a numerical integration routine results in considerably higher computation efficiency for SBE compared to the Madelin and Kratzer simulators; numerical integration routines of packages such as MATLAB has been developed over decades to dynamically adjust simulation step-sizes according to time-varying inputs. Thus the simulation of spin-3/2 dynamics with time-varying RF or gradients is best approached using the SBE formalism.

The behaviour of the SBE has been demonstrated through simulations, including the expected negligible difference between SBE and BE for fluid regions. However, for biological tissue environments, the deviations between spin-3/2 and spin-1/2 dynamics are more pronounced, and depend on the specifics of the pulse sequence, necessitating a functional form for the spin system that elucidates meaning. For applications requiring accurate predictions, such as ^{23}Na-MRF, the SBE will be a crucial tool. Indeed, the recent results of Kratzer et al (18) confirm the performance gain from using the ISTO-based simulation of (12), compared with their previous proof-of-concept study (10) using BE-based simulation. With the full description of the ^{23}Na spin dynamics, the SBE can be used for the biological environments in which the residual quadrupolar frequency is large, such as cartilage.

Conclusions

The 'Spin-3/2 Bloch Equation' has been formulated as a generalised representation of spin-3/2 dynamics in biological tissue environments, encapsulating excitation, relaxation and off resonance

effects for an intuitive, structured system representation that facilitates accurate and computationally efficient simulation for pulse sequence design.

References

1. Madelin G, Kline R, Walvick R, Regatte RR. A method for estimating intracellular sodium concentration and extracellular volume fraction in brain in vivo using sodium magnetic resonance imaging. Scientific Reports 2014; 4:4763.

2. Madelin G, Regatte RR. Biomedical applications of sodium MRI in vivo. Journal of Magnetic Resonance Imaging 2013; 38:511–529.

3. Ouwerkerk R, Morgan RH. ^{23}Na MRI: from research to clinical use. J Am Coll Radiol 2007; 4:739–741.

4. Madelin G, Babb J, Xia D, Chang G, Krasnokutsky S, Abramson SB, Jerschow A, Regatte RR. Articular cartilage: evaluation with fluid-suppressed 7.0-T sodium MR imaging in subjects with and subjects without osteoarthritis. Radiology 2013; 268:481–491.

5. Shymanskaya A, Worthoff WA, Stoffels G, Lindemeyer J, Neumaier B, Lohmann P, Galldiks N, Langen KJ, Shah NJ. Comparison of [^{18}F] fluoroethyltyrosine PET and sodium MRI in cerebral gliomas: A pilot study. Molecular Imaging and Biology 2020; 22:198–207.

6. Tanase C, Boada FE. Algebraic description of spin 3/2 dynamics in NMR experiments. Journal of Magnetic Resonance 2005; 173:236–253.

7. Fleysher L, Oesingmann N, Inglese M. B_0 inhomogeneity-insensitive triple-quantum-filtered sodium imaging using a 12-step phase-cycling scheme. NMR in Biomedicine 2010; 23:1191–1198.

8. Hoesl MA, Schad LR, Rapacchi S. Efficient (^{23}Na) triple-quantum signal imaging on clinical scanners: Cartesian imaging of single and triple-quantum (^{23}Na) (CRISTINA). Magnetic resonance in medicine 2020; 84:2412–2428.

9. Kharrazian R, Jakob PM. Dynamics of ^{23}Na during completely balanced steady-state free precession. Journal of Magnetic Resonance 2006; 179:73–84.

10. Kratzer FJ, Flassbeck S, Nagel AM, Behl NG, Knowles BR, Bachert P, Ladd ME, Schmitter S. Sodium relaxometry using ^{23}Na MR fingerprinting: A proof of concept. Magnetic Resonance in Medicine 2020; 84:2577–2591.

11. Madelin G, Lee JS, Inati S, Jerschow A, Regatte RR. Sodium inversion recovery MRI of the knee joint in vivo at 7T. Journal of Magnetic Resonance 2010; 207:42–52.

12. Hancu I, van der Maarel JRC, Boada FE. A model for the dynamics of spins 3/2 in biological media: Signal loss during radiofrequency excitation in triple-quantum-filtered sodium MRI. Journal of Magnetic Resonance 2000; 147:179–191.

13. Tsang A, Stobbe RW, Beaulieu C. Triple-quantum-filtered sodium imaging of the human brain at 4.7 T. Magnetic Resonance in Medicine 2012; 67:1633–1643.

14. Stobbe R, Beaulieu C. In vivo sodium magnetic resonance imaging of the human brain using soft inversion recovery fluid attenuation. Magnetic Resonance in Medicine 2005; 54:1305–1310.

15. Feldman RE, Stobbe R, Watts A, Beaulieu C. Sodium imaging of the human knee using soft inversion recovery fluid attenuation. Journal of Magnetic Resonance 2013; 234:197–206.

16. Lee JS, Regatte RR, Jerschow A. Optimal excitation of ^{23}Na nuclear spins in the presence of residual quadrupolar coupling and quadrupolar relaxation. The Journal of Chemical Physics 2009; 131:174501.

17. Gilles A, Nagel AM, Madelin G. Multipulse sodium magnetic resonance imaging for multicompartment quantification: Proof-of-concept. Scientific Reports 2017; 7:17435.

18. Kratzer FJ, Flassbeck S, Schmitter S, Wilferth T, Magill AW, Knowles BR, Platt T, Bachert P, Ladd ME, Nagel AM. 3D sodium (^{23}Na) magnetic resonance fingerprinting for time-efficient relaxometric mapping. Magnetic Resonance in Medicine 2021; .

19. van der Maarel JR. Thermal relaxation and coherence dynamics of spin 3/2. I. Static and fluctuating quadrupolar interactions in the multipole basis. Concepts in Magnetic Resonance 2003; 19A:97–116.

20. van der Maarel JR. Thermal relaxation and coherence dynamics of spin 3/2. II. Strong radiofrequency field. Concepts in Magnetic Resonance 2003; 19A:117–133.

21. Chapman BE, Naumann C, Philp DJ, Eliav U, Navon G, Kuchel PW. z-spectra of ^{23}Na+ in stretched gels: Quantitative multiple quantum analysis. Journal of Magnetic Resonance 2010; 205:260–268.

22. Bowden GJ, Hutchison WD. Tensor operator formalism for multiple-quantum NMR: 1. spin-1 nuclei. Journal of Magnietc Resonance 1986; 67:415–437.

23. Bowden GJ, Hutchison WD. Tensor operator formalism for multiple-quantum NMR: 2. spins-3/2, 2 and 5/2 and general I. Journal of Magnetic Resonance 1986; 67:415–437.

24. Liesen J, Mehrmann V. "Linear algebra", pp. 85–86. Springer, 2015.

25. Garren KR. "Bounds for the Eigenvalues of a Matrix", Vol. 4373, pp. 6–7. National Aeronautics and Space Administration, 1968.

26. Rooney WD, SpringerJr CS. The molecular environment of intracellular sodium: ^{23}Na NMR relaxation. NMR in Biomedicine 1991; 4:227–245.

27. Shekar SC, Tang JA, Jerschow A. Dynamics of I=3/2 nuclei in isotropic slow motion, anisotropic and partially ordered phases. Concepts in Magnetic Resonance Part A 2010; 36:362–387.

28. Wilferth T, Gast LV, Stobbe RW, Beaulieu C, Hensel B, Uder M, Nagel AM. ^{23}Na MRI of human skeletal muscle using long inversion recovery pulses. Magnetic Resonance Imaging 2019; 63:280–290.

29. Hancu I, Boada FE, Shen GX. Three-dimensional triple-quantum-filtered ^{23}Na imaging of in vivo human brain. Magnetic Resonance in Medicine 1999; 42:1146–54.

Figures and Tables

Figure 1: The SBE system matrix, **L**, colour-coded to indicate source of terms: Red-shaded entries are associated with RF excitation; Yellow-shaded entries are off-resonance terms; Green-shaded terms are associated with residual quadrupolar oscillation; Blue-shaded terms are associated with the fluctuating quadrupolar interaction.

Figure 2: (a) The simulated time evolution of on-resonance ^{23}Na longitudinal magnetisation during a 10-ms rectangular pulse. (b) The dependence of longitudinal magnetisation on the rectangular pulse length. Kratzer and Madelin simulators were each run with 3000 time-steps.

Figure 3: Simulated time evolution of on-resonance ^{23}Na (a) longitudinal magnetisation during the WURST IR pulse in saline, agar and xanthan, and (b) transverse magnetisation in xanthan. SBE simulation depicting (c) the amplitude of the longitudinal magnetisation during the inversion preparation stage of the WURST IR pulse with the influence of B_0 inhomogeneity, and (d) amplitude values at the end of the stage.

Figure 4: (a-h) Evolution of the rank-1 and rank-3 coherences of xanthan during the three-pulse TQF experiment. (i) The summed coherences of the phase cycling steps. The red bars indicate periods of RF excitation.

Table 1: Simulation run times of ^{23}Na in xanthan during WURST IR pulse.

Simulator	**Solver**	**Number of steps**	**Run time (ms)**[a]
SBE	ode45	300[b]	50±11
Kratzer et al (2021)	Eigen-decomposition method with linearly discretised time steps	3000	678±28
		1000	237±30
		300	71±10
Madelin et al (2014)	Consecutive operations (ω_1, ω_Q, ω_Δ, relaxation) with linearly discretised time steps	3000	1277±62
		1000	421±26
		300	133±25

[a] The measurements were repeated 100 times

[b] Note that the user-defined number of steps in the call to ode45 does not determine the step size chosen internally within the integration routine. The algorithm returns output that is interpolated to the user-defined number of steps.

Supporting Information Figure S1: Evolution of the rank-2 coherences of xanthan during the three-pulse TQF experiment.

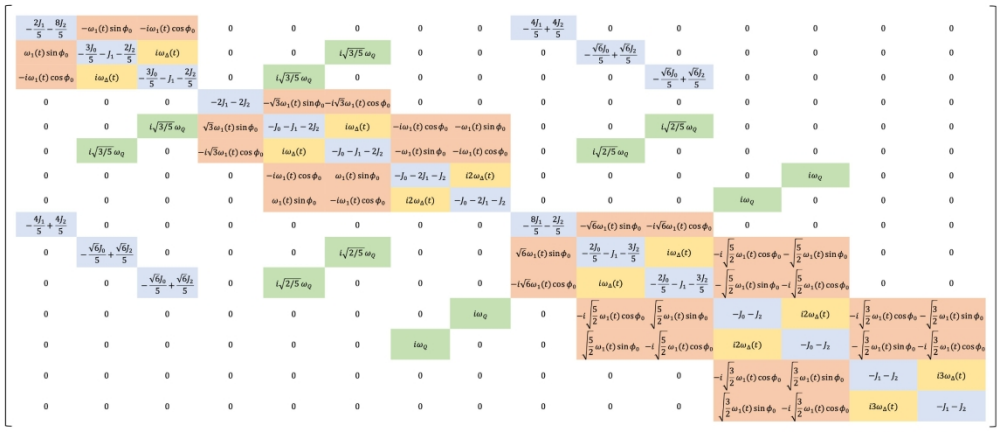

Fig. 1. The SBE system matrix, **L**, colour-coded to indicate source of terms: Red-shaded entries are associated with RF excitation; Yellow-shaded entries are off-resonance terms; Green-shaded terms are associated with residual quadrupolar oscillation; Blue-shaded terms are associated with the fluctuating quadrupolar interaction.

208x93mm (600 x 600 DPI)

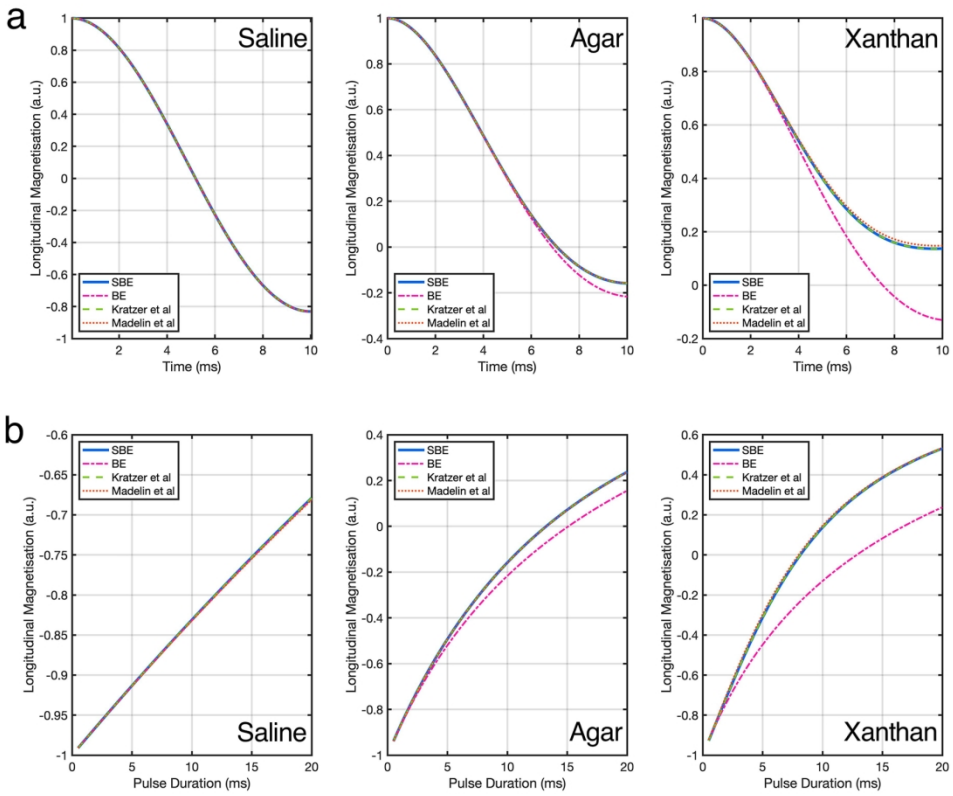

Fig. 2. (a) The simulated time evolution of on-resonance ^{23}Na longitudinal magnetisation during a 10-ms rectangular pulse. (b) The dependence of longitudinal magnetisation on the rectangular pulse length. Kratzer and Madelin simulators were each run with 3000 time-steps.

163x138mm (600 x 600 DPI)

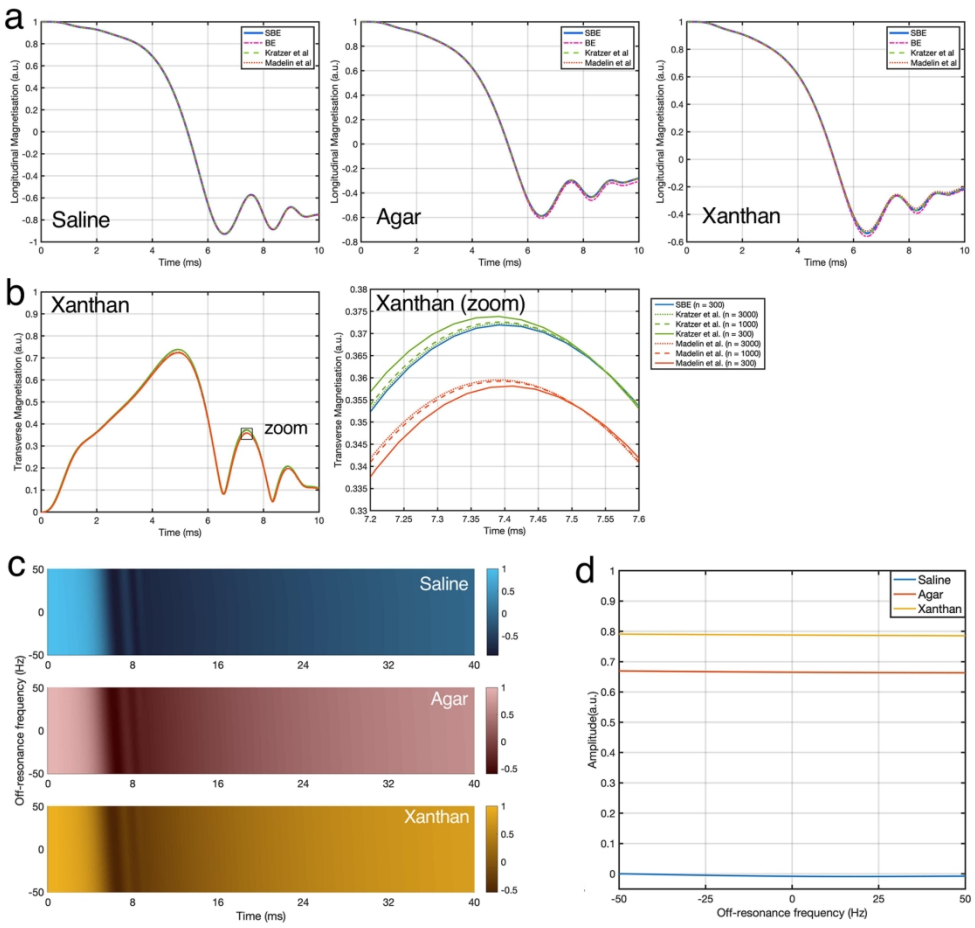

Fig. 3. Simulated time evolution of on-resonance ^{23}Na (a) longitudinal magnetisation during the WURST IR pulse in saline, agar and xanthan, and (b) transverse magnetisation in xanthan. SBE simulation depicting (c) the amplitude of the longitudinal magnetisation during the inversion preparation stage of the WURST IR pulse with the influence of B_0 inhomogeneity, and (d) amplitude values at the end of the stage.

167x164mm (600 x 600 DPI)

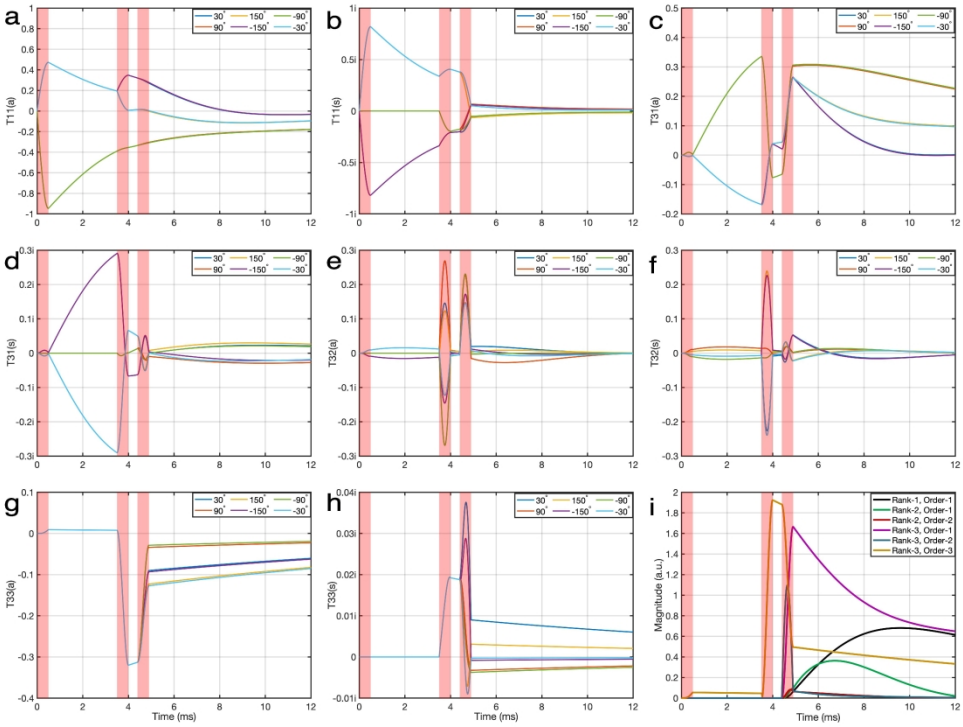

Fig. 4. (a-h) Evolution of the rank-1 and rank-3 coherences of xanthan during the three-pulse TQF experiment. (i) The summed coherences of the phase cycling steps. The red bars indicate periods of RF excitation.

204x152mm (600 x 600 DPI)

Supporting Information

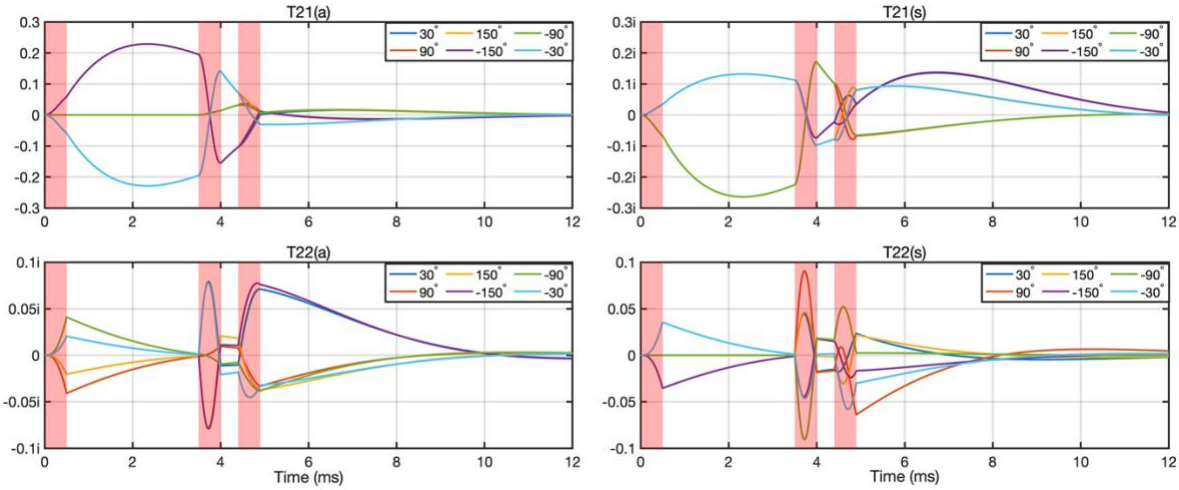

Supporting Information Figure S1: Evolution of the rank-2 coherences of xanthan during the three-pulse TQF experiment.

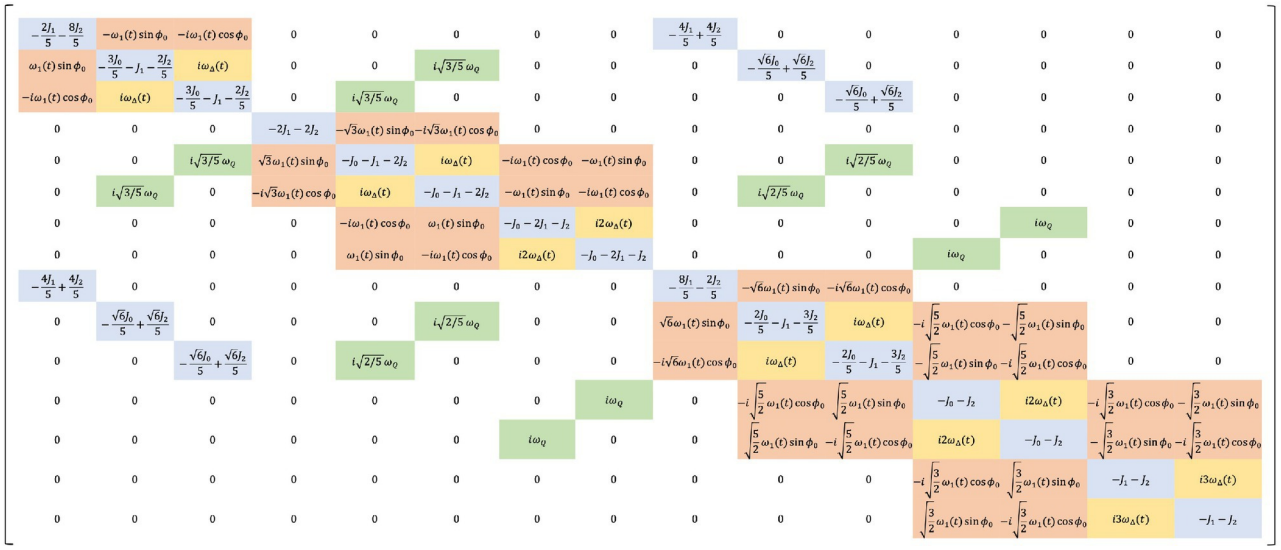

mrm_29276_fig1.eps

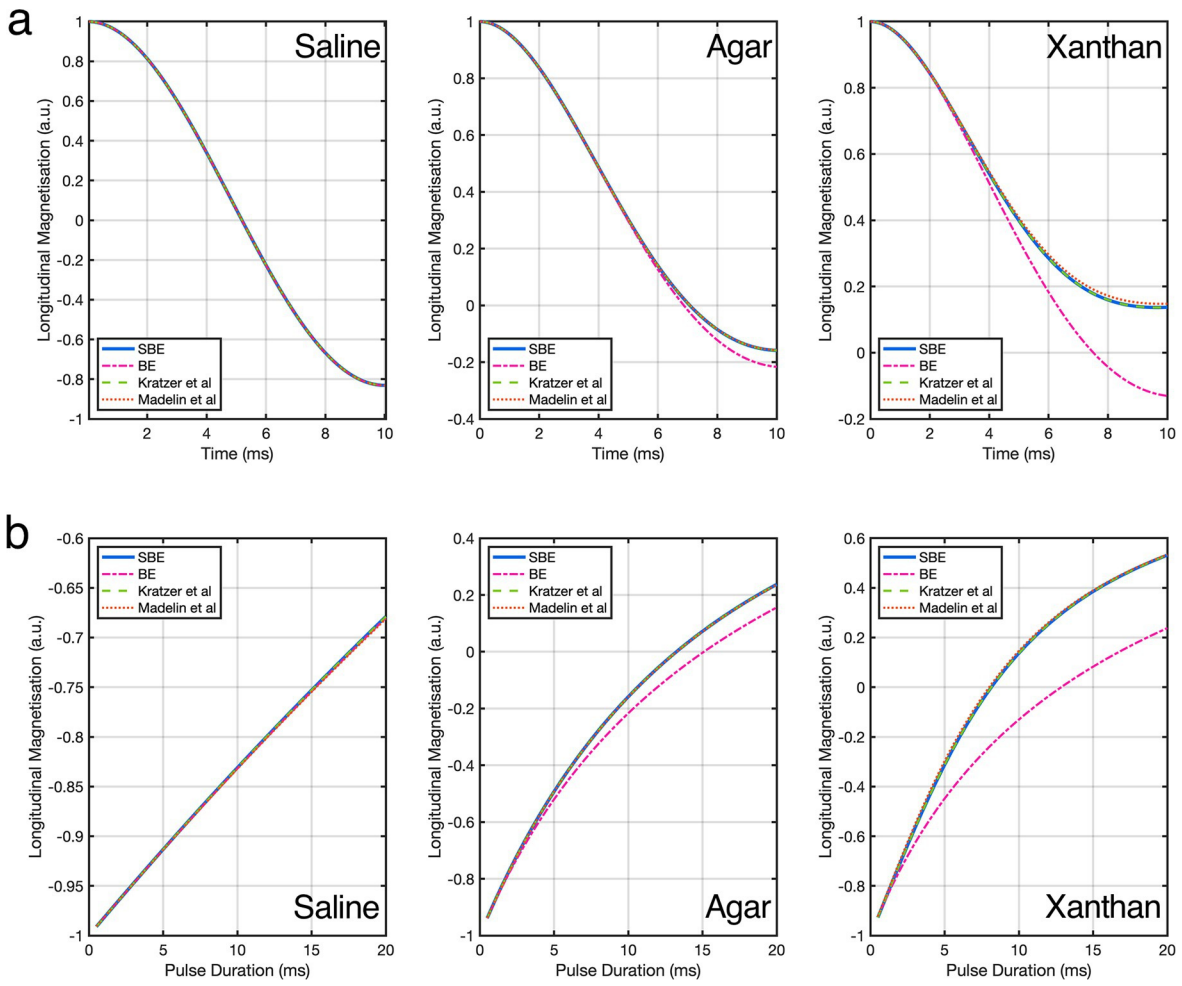

mrm_29276_fig2.eps

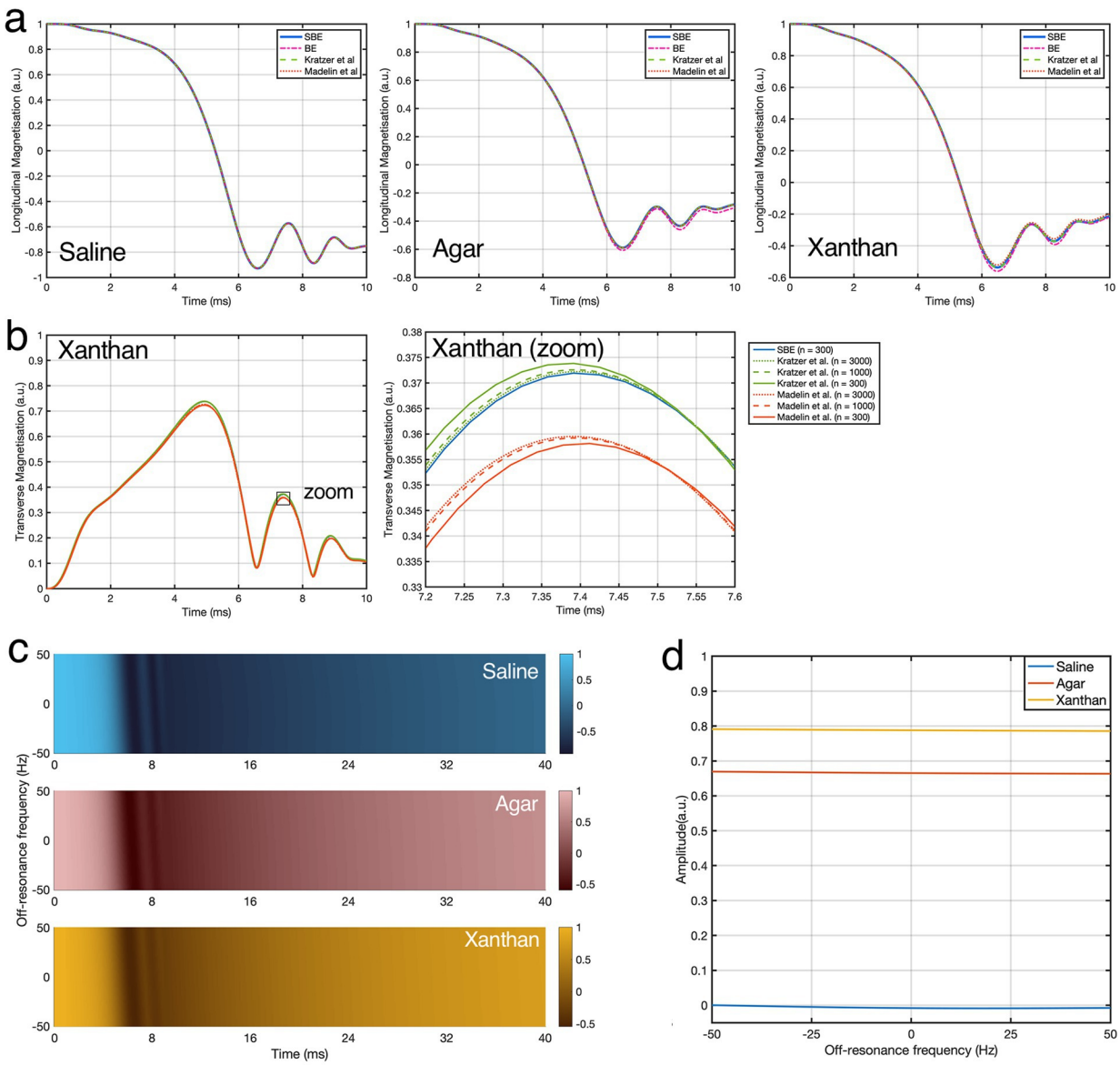

mrm_29276_fig3.eps

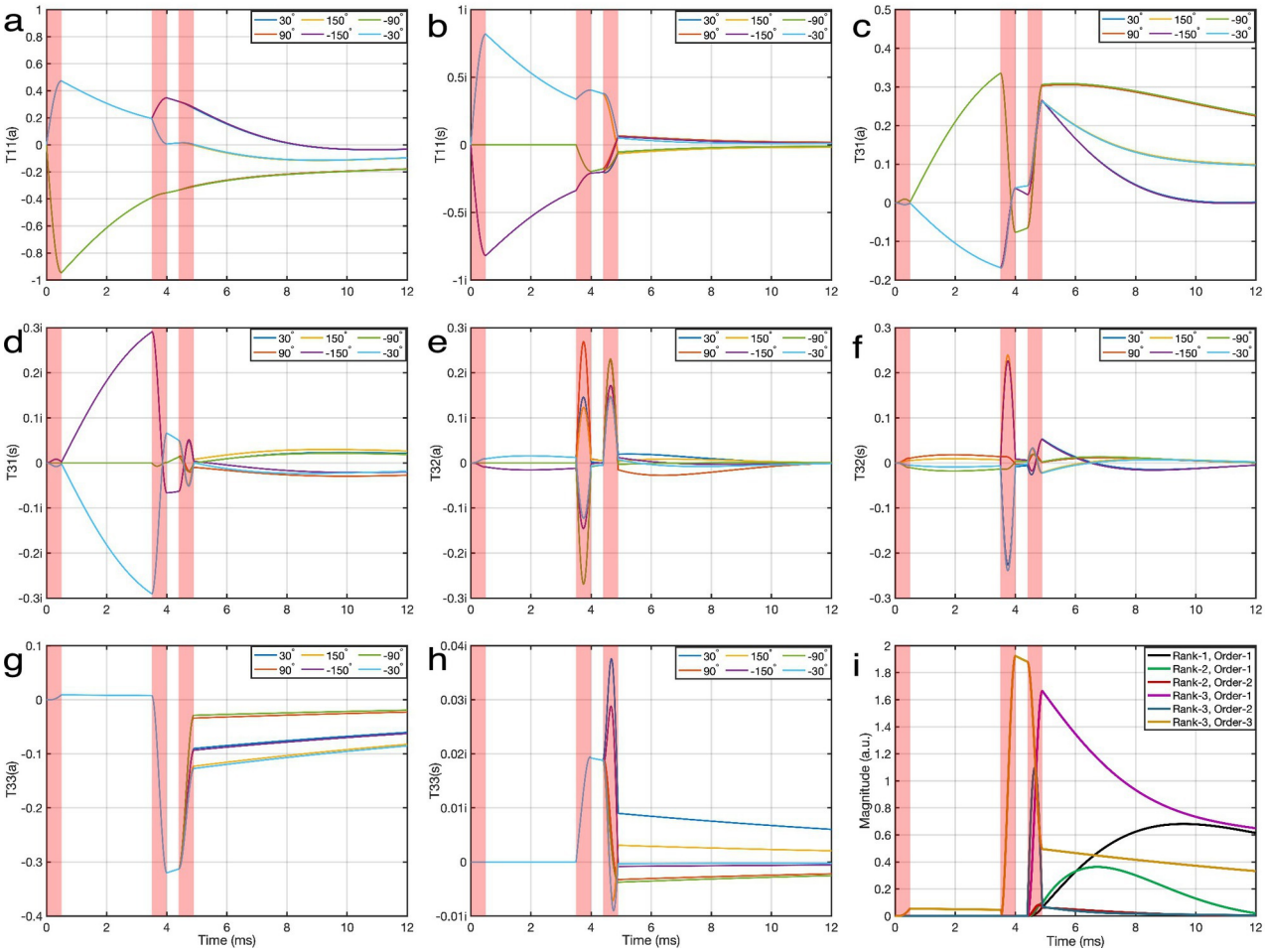

mrm_29276_fig4.eps